Long non-coding RNA RP11-196G11.6 inhibits neuroblastoma progression by regulating the miR-376a-3p/RYBP signaling axis

JIE ZHANG[1,2], KAI HUANG[1], JIANWU ZHOU[1], WENGE LIAO[1], FEI LI[2], ZHENZHEN ZHAO[1] and SHAN WANG[1]

[1]Department of Pediatric Surgical Oncology, The Children's Hospital of Chongqing Medical University, National Clinical Research Center for Child Health and Disorders, Ministry of Education Key Laboratory of Child Development and Disorders, Chongqing Key Laboratory of Pediatric Metabolism and Inflammatory Diseases, Chongqing 400014, P.R. China; [2]Department of Pediatric Surgery, Guizhou Provincial People's Hospital, Guiyang, Guizhou 550002, P.R. China

Received June 30, 2025; Accepted October 7, 2025

DOI: 10.3892/ol.2025.15376

Abstract. Long non-coding RNAs (lncRNAs) are emerging as key regulators of neuroblastoma (NB) progression; however, their interplay with MYCN-driven mechanisms remains to be elucidated. The present study aimed to characterize the expression profile of lncRNA RP11-196G11.6 in NB, and to further explore its functional role and mechanism in the pathogenesis of this disease. Transcriptomics data from NB and disseminated tumor cell (DTC) samples (Gene Expression Omnibus; accession no. GSE94035) were analyzed via principal component analysis (PCA), differential expression analysis and CIBERSORT immune profiling. The biological function was assessed using gain- and loss-of-function experiments in IMR-32 ($MYCN^+$) and SH-SY5Y ($MYCN^-$) cells. Dual-luciferase reporter assays were performed to identify the interaction between RP11-196G11.6, microRNA (miR)-376a-3p and RING1 and YY1-binding protein (RYBP). Rescue experiments were performed by co-transfecting RP11-196G11.6-overexpressing cells with a miR-376a-3p mimic to identify the hypothetical regulatory role of RP11-196G11.6 in NB progression *in vitro*. The present analysis results demonstrated that the PCA could distinguish tumor and DTC samples, with MYCN amplification driving distinct clustering in tumors but not in DTCs. Differential expression analysis based on $MYCN^{+/-}$ in both tumor and DTC groups identified 161 differentially expressed lncRNAs (73 upregulated and 88 downregulated). Notably, RP11-196G11.6 was highly expressed in $MYCN^+$ tumors, and silencing RP11-196G11.6 promoted the viability, migration, invasion and epithelial-mesenchymal transition in $MYCN^+$ cells, whereas RP11-196G11.6 overexpression induced the opposite effects in $MYCN^-$ cells. Mechanistically, RP11-196G11.6 directly inhibited miR-376a-3p, which targeted RYBP. Overexpression of miR-376a-3p reversed the tumor suppressor phenotype driven by RP11-196G11.6. In summary, the present study demonstrated that RP11-196G11.6 may inhibit NB progression by sponging miR-376a-3p, leading to the upregulation of RYBP expression and consequently inhibiting NB progression. These findings revealed a novel lncRNA-miRNA axis involved in NB pathogenesis.

Correspondence to: Dr Shan Wang, Department of Pediatric Surgical Oncology, The Children's Hospital of Chongqing Medical University, National Clinical Research Center for Child Health and Disorders, Ministry of Education Key Laboratory of Child Development and Disorders, Chongqing Key Laboratory of Pediatric Metabolism and Inflammatory Diseases, 136 Zhongshan 2nd Road, Yuzhong, Chongqing 400014, P.R. China
E-mail: wangshan@hospital.cqmu.edu.cn; wanshan778@163.com

Key words: neuroblastoma, long non-coding RNA, RP11-196G11.6, epithelial-mesenchymal transition, MYCN

Introduction

Neuroblastoma (NB) is the most common extracranial solid tumor in children and accounts for 3-10% of cases of childhood cancer mortality (1-3). The prognosis markedly varies, with overall survival ranging from >95% for low-risk patients to <40% for high-risk patients (4). The treatment plan for NB is mainly based on the degree of risk expected at the time of diagnosis, with risk assessment including various factors, such as age, International Neuroblastoma Staging System (INSS) stage/International Neuroblastoma Risk Group stage (5,6), MYCN amplification status, International Neuroblastoma Pathology Classification (7), histological category, grade of tumor differentiation, DNA ploidy and 11q deletion (8). Among them, MYCN amplification status (9) and metastasis (10) are the key reasons for treatment failure.

MYCN is a highly conserved human oncogene and numerous studies have confirmed that MYCN gene status is associated with various types of cancer, particularly NB (11,12), and is key for the prediction of patient prognosis and guiding treatment. Compared with in patients with NB without MYCN amplification ($MYCN^-$), those with MYCN amplification ($MYCN^+$) have been reported to have an increased probability of metastasis (13).

Long non-coding RNAs (lncRNAs) serve key roles in the proliferation, differentiation and migration of malignant tumor cells by competitively binding to microRNAs (miRNAs/miRs) as competitive endogenous RNAs and then regulating the

expression of target genes, and the differentiation and migration of malignant tumor cells (14). Previous studies have reported an association between MYCN and lncRNAs. For example, the lncRNA AC142119.1 has been reported to be markedly upregulated in $MYCN^+$, advanced INSS and high-risk NB tissues, and is associated with poor survival in patients with NB. Furthermore, increased expression levels of AC142119.1 can enhance NB cell proliferation *in vitro* and *in vivo* (15). High expression levels of the lncRNA small nucleolar RNA host gene 1 (SNHG1) are associated with a poor prognosis and MYCN status in NB. Downregulation of SNHG1 levels in the $MYCN^+$ NB cell line SK-N-BE2 have been shown to result in the inhibition of cell proliferation and colony-forming ability (16). In addition, elevated levels of nuclear paraspeckle assembly transcript 1 (NEAT1) expression in NB cells and tissues are associated with advanced pathological stages and poor prognosis, whereas NEAT1 silencing inhibits NB proliferation *in vivo*. Mechanistically, NEAT1 acts as a competitive sponge for miR-873-5p and regulates MYCN and polypeptide N-acetylgalactosaminyltransferase I level (17). These studies suggest that lncRNAs serve key roles in the progression of $MYCN^+$ NB.

In the present study, bioinformatics analyses were performed on different NB samples to identify the differentially expressed lncRNAs (DElncRNAs) that were associated with MYCN and their functions were analyzed. CIBERSORT was used to identify MYCN-regulated regulatory T cells (Tregs) and T follicular helper cells (Tfhs). To identify the DElncRNAs associated with Tregs and Tfhs, Spearman's rank correlation coefficient was further computed using the DElncRNA expression levels, and the proportions of Tregs and Tfhs. On this basis, the lncRNA RP11-196G11.6 was selected. The effects of miR-376a-3p and its downstream target genes mediated by RP11-196G11.6 on the viability, migration and invasion of NB cells were further verified. The aim of the present study was to elucidate the specific mechanisms by which RP11-196G11.6 acts as a tumor suppressor in NB, and to establish a potential novel target for the diagnosis and treatment of NB.

Materials and methods

Clinical specimens and public data. Public transcriptome-sequence data files from patients with NB, comprising tumor samples (n=16) and disseminated tumor cells (DTC) (n=42) [Gene Expression Omnibus (GEO); accession no. GSE94035; https://www.ncbi.nlm.nih.gov/geo/query/acc.cgi?acc=GSE94035] -were downloaded from the Sequence Read Archive (SRA; https://www.ncbi.nlm.nih.gov/sra?term=SRP097735). The National Center for Biotechnology Information SRA Tool FASTQ-dump (https://github.com/ncbi/sra-tools/wiki/02.-Installing-SRA-Toolkit) was used to convert the SRA Run files to FASTQ format. FASTX-Toolkit (version 0.0.13; http://hannonlab.cshl.edu/fastx_toolkit/) was used to trim the raw reads of low-quality bases. The clean reads were subsequently evaluated using FastQC (Version 0.12.0) (http://www.bioinformatics.babraham.ac.uk/projects/fastqc/).

Reads alignment and differentially expressed gene (DEG) analysis. The clean reads were aligned with the human GRch38 genome via 'tophat2' (Version 2.1.1), allowing four mismatches (18). Several core bioinformatics analyses, including DEG analysis, immune cell-type quantification and principal component analysis (PCA), were implemented using the R programming environment (Version 4.3.2; https://cran.r-project.org/). The unique mapped reads were ultimately used to calculate the read number and the reads/kb of exon per million fragments mapped (RPKM) for each gene. The RPKM values were used to assess gene expression levels. 'edgeR' (Version 4.6.3) (19), a software tool specifically designed to analyze the differential expression of genes, was applied to screen the RNA-sequencing data for DEGs (including lncRNA and mRNA). The results were analyzed according to the following criteria: Fold change ≥ 2 or ≤ 0.5, and false discovery rate (FDR) ≤ 0.05, to determine whether genes were differentially expressed.

lncRNA prediction and direction identification. A pipeline for lncRNA identification similar to that described in a previous study was used to systematically understand the lncRNA expression of NB tumor samples and DTC samples (20), which was constructed via Cufflinks software (Version 2.2.1) (21). All the steps of the pipeline are shown in Fig. 1A. Based on the NB GSE94035 dataset, samples from the DTC group ($MYCN_{amplified}$ n=13, $MYCN_{non\text{-}amplified}$ n=23) and the tumor group ($MYCN_{amplified}$ n=10, $MYCN_{non\text{-}amplified}$ n=6) were included. The edgeR software (Version 4.6.3) was used to analyze the differential expression of mRNAs and lncRNAs between DTCs and tumors. Then, using the immunedeconv package (Version 2.0.3) (22), a lncRNA immunoregulatory network was constructed. Furthermore, the infiltration levels of 22 immune cell subtypes were quantified using CIBERSORT (Version 2020; https://cibersortx.stanford.edu/) and intergroup differences were compared. Through integrated analysis, key lncRNAs were identified among the DElncRNAs that not only participate in immunoregulatory networks but also demonstrate significant associations with specific immune cell infiltration levels. Potential miRNAs interacting with the target lncRNA were predicted using miRanda (https://cloud.oebiotech.cn/task/detail/array_miranda_plot/), while the potential target genes binding to these miRNAs were identified via miRDB (https://mirdb.org/).

Weighted gene co-expression network analysis (WGCNA) and co-expression analysis. To fully understand gene expression patterns, WGCNA (23) was used to cluster genes with similar expression patterns and the default parameters were used. All expressed genes were used as input data. The eigengenes of each clustering module were regarded as the representative expression pattern of the gene in each module. To explore the regulatory mode between lncRNAs and their host mRNAs, Pearson's rank correlation coefficients were computed, which were used to divide their relationships into the following three categories: i) Positively correlated; ii) negatively correlated; and iii) non-correlated. Cutoffs of $P \leq 0.01$ and Pearson coefficient >0.8 were applied to identify the co-expression pairs.

Functional enrichment analysis. To determine the functional categories of the DEGs, the KOBAS 2.0 server was used to identify the enriched Gene Ontology (GO) terms (24). The

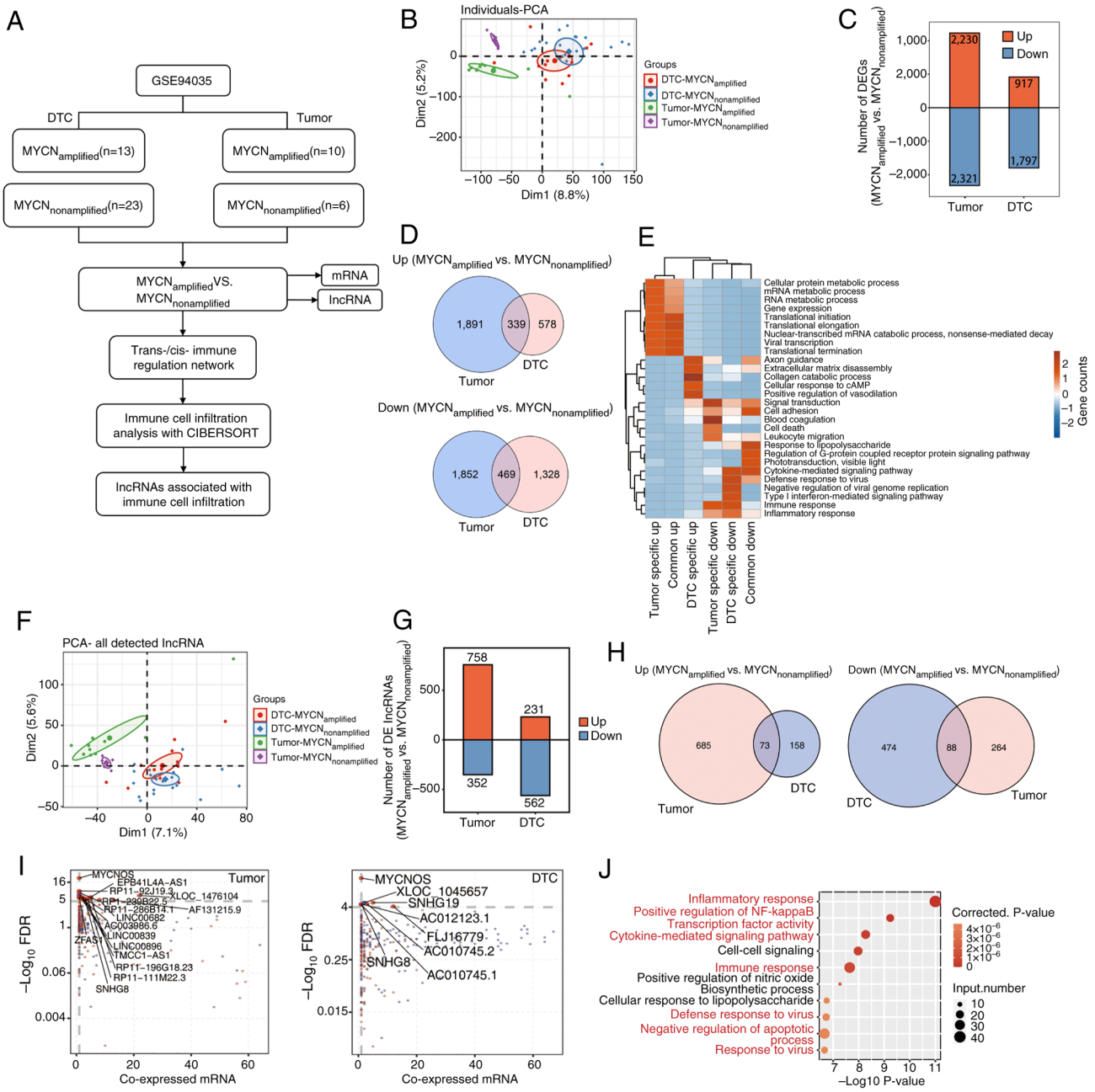

Figure 1. Analysis of DElncRNAs in tumor and bone marrow metastatic tissues. (A) Schematic diagram of the bioinformatics analysis process. (B) PCA between tumor and DTC samples, and between MYCN amplification statuses. (C) Analysis of DEGs between MYCN$^+$ and MYCN$^-$ samples in tumor and DTC samples. (D) Venn diagrams depicting commonly upregulated and downregulated DEGs in the four groups of samples. (E) GO enrichment analysis showing the GO terms that were most significantly enriched in 808 DEGs. The color scale represents the enrichment intensity of gene sets across different groups, based on the number of genes enriched in each pathway and normalized to a range of -2 to 2. (F) PCA of the lncRNAs among the DEGs. (G) DElncRNA analysis between MYCN$^+$ and MYCN$^-$ samples in tumor and DTC samples. (H) Venn diagrams indicating commonly upregulated and downregulated DElncRNAs in the four groups of samples. (I) Weighted gene co-expression network analysis and co-expression analysis. Scatter plots of DElncRNAs and their co-expressed DEmRNAs in MYCN$^+$ vs. MYCN$^-$ samples across tumor and DTC cohorts. Red points denote upregulated lncRNAs involved in co-expression pairs and blue points denote downregulated lncRNAs. The straight lines represent correlations between the two variables. Cutoffs of P≤0.01 and Pearson coefficient >0.8 were applied to identify the co-expression pairs. (J) Top 10 most enriched GO terms (biological processes) in DEmRNAs co-expressed with the DElncRNAs; the highlighted terms in red are associated with immune and inflammatory responses. lncRNA, long non-coding RNA; PCA, principal component analysis; DTC, disseminated tumor cell; DEG, differentially expressed gene; GO, Gene Ontology; DElncRNA, differentially expressed lncRNA; DEmRNA, differentially expressed mRNA; FDR, false discovery rate.

enrichment of each term was defined via a hypergeometric test and the Benjamini-Hochberg FDR controlling procedure.

Cell-type quantification. The R (Version 4.3.2; https://cran.r--project.org/) package 'immunedeconv (Version 2.0.3)' provides a unified interface for seven deconvolution methods to estimate immune cell fractions, with the EPIC and CIBERSORT methods applied in the present study.

MYCN-associated lncRNA-immune cell infiltration network. The Spearman correlation coefficient was used to assess the correlation between the expression levels of DElncRNAs and

the ratio of Tregs to Tfhs. lncRNA-cell pairs with Spearman correlation coefficients of >0.6 (or <-0.6) and a corresponding P-value (Benjamini-Hochberg corrected) of <0.01 were considered significantly correlated. A lncRNA-immune cell infiltration network was constructed with Cytoscape (Version 3.10.4; https://cytoscape.org/).

PCA and Venn diagram. PCA was performed using the R package 'factoextra' (Version 1.0.7; https://cloud.r-project.org/package=factoextra) to display the clusters of samples with the first two components. After the reads of each gene in the samples were standardized by tags/million, the internal script was used for the visualization of next-generation sequencing data and genome annotations. The Venn diagram was generated using Venny (Version 2.1; https://bioinfogp.cnb.csic.es/tools/venny/;) with gene lists from $MYCN^+$ and $MYCN^-$ tumor and DTC samples inputted for comparative analysis.

Fluorescence in situ hybridization (FISH). Between March and May 2025, $MYCN^+$ and $MYCN^-$ tumor samples (n=5/group) were collected retrospectively from the Department of Pathology, Guizhou Provincial People's Hospital (Guiyang, China). The cohort comprised 10 children (7 male and 3 female patients) aged between 5 months and 12 years old, with an mean age of 4.58 years. The inclusion criteria were as follows: i) Pathological confirmation of NB following surgery; ii) availability of adequate resected tissue specimens; iii) genetic testing to determine MYCN amplification status. Patients failing to meet any of these criteria were excluded. Following resection, all tumor tissues were fixed in 4% paraformaldehyde at room temperature for 24 h, followed by paraffin embedding. Then, tissue sections (6 μm) were mounted on positively charged slides and stored at 4˚C until use. The expression levels of RP11-196G11.6 and U6 in tumor samples were detected using a customized RP11-196G11.6 FISH detection kit [cat. no. Mk1257-H (CY3); Wuhan Boster Biological Technology, Ltd.]; all reagents including antibodies used prior to DAPI staining were sourced from this kit. Briefly, after deparaffinization and rehydration of the slides, target nucleic acids were exposed by digestion with pepsin (3% citric acid-diluted) for 20 min at 37˚C. This was followed by washes with PBS and distilled water. Post-fixation was carried out using 1% paraformaldehyde containing 0.1% diethyl pyrocarbonate for 10 min at room temperature. Pre-hybridization was performed at 42˚C for 4 h in a humidified chamber containing 20% glycerol. A 20-μl hybridization solution containing the RP11-196G11.6 oligonucleotide probe (primary antibody) was added to the sample under a coverslip and incubated at 42˚C overnight. Post-hybridization washes included 2X SSC (5 min twice), 0.5X SSC (15 min) and 0.2X SSC (15 min) at 37˚C. Subsequently, the sections were blocked and incubated with biotinylated mouse anti-digoxigenin (secondary antibody) at 37˚C for 1 h, washed with PBS and treated with SABC-Cy3 at 37˚C for 1 h. After the final PBS washes, the nuclei were counterstained with DAPI (cat. no. KGA215-50;Nanjing KGI Biological Technology Development Co., Ltd.). The images were captured via fluorescence microscopy (DAPI and CY3 channels; CKX53; Olympus Corporation), and image analysis was performed using ImageJ (version 1.53q; National Institutes of Health). Background correction was performed using five cell-free regions. Nuclei were identified via Otsu's thresholding and watershed segmentation (excluding abnormal/incomplete nuclei). CY3 integrated density (IntDen) was measured within nuclear regions of interest and normalized to nuclear area, which was defined by nuclear segmentation performed on DAPI channel images, using the following formula: Normalized intensity=(CY3 IntDen-Background)/Nuclear Area. Measurements were verified across three non-overlapping fields. Normalized intensity values were compared between $MYCN^+$ and $MYCN^-$ groups.

Cell culture and transfection. SH-SY5Y (cat. no. iCell-h187; iCell Bioscience, Inc.), IMR-32 (cat. no. CL-0124; Procell Life Science & Technology Co., Ltd.) and 293T (cat. no. CL-0005; Procell Life Science & Technology Co., Ltd.) cells were confirmed by short tandem repeat profiling. IMR-32 and SH-SY5Y cells were cultured in MEM (cat. no. 11090081; Gibco; Thermo Fisher Scientific, Inc.), and 293T cells were cultured in DMEM (cat. no. 11965092; Gibco; Thermo Fisher Scientific, Inc.) supplemented with 10% FBS (cat. no. 10100147C; Gibco: Thermo Fisher Scientific, Inc.) and 1% penicillin-streptomycin (cat. no. 15140122;Gibco; Thermo Fisher Scientific, Inc.). The cells were cultured in a cell incubator at 37˚C and 5% CO_2.

IMR-32 and SH-SY5Y cells were transfected at 70% confluence using Lipofectamine® 3000 Transfection Kit (cat. no. L3000150; Invitrogen; Thermo Fisher Scientific, Inc.) according to the manufacturer's protocol. Briefly, for each well of a 6-well plate, 2.5 μg RP11-196G11.6 overexpression vector [oe-RP11; pcDNA3.1(+) vector utilized as the plasmid backbone], 3.3 μg RP11-196G11.6 small interfering (si)RNA [si-RP11 (125 μl/1OD)] or 0.4 μg mimics (20 μmol/l) were diluted in 125 μl Opti-MEM with 5 μl P3000 reagent, whereas 5 μl Lipofectamine 3000 was diluted in 125 μl Opti-MEM. After 5 min incubation at 37˚C, the two solutions were combined, incubated for 15 min at 37˚C and added to cells in serum-free medium. Following 6 h transfection, the medium was supplemented with complete medium containing 20% FBS, and cells were analyzed after 48 h of incubation at 37˚C. The si-RP11, oe-RP11, miR-376a-3p mimic and corresponding controls were all provided by Jiangxi Zhonghong Boyuan Biotechnology Co., Ltd. Transfection was performed according to the instructions of the Lipofectamine 3000 Transfection Kit. Briefly, si-RP11 and si-negative control (NC) were transfected into IMR-32 cells; and oe-RP11 and oe-NC were transfected into SH-SY5Y cells. To assess whether RP11-196G11.6 mediates its effect on NB cells by regulating the expression of miR-376a-3p, SH-SY5Y cells were co-transfected with oe-RP11 or oe-NC, and the miR-376a-3p mimic or mimic NC. The sense and antisense sequences of the si-RP11 and si-NC, together with the sequences of the hsa-miR-376a-3p mimic and mimic NC, are detailed in Table I.

Reverse transcription-quantitative PCR (RT-qPCR). Cellular total RNA was extracted using the miRNA Extraction Kit (cat. no. CWY113S; CWBio) for miRNA, and the Ultrapure RNA Kit (cat. no. CW0581M; CWBio) for lncRNA and mRNA. Subsequently, cDNA was synthesized from the respective RNA fractions using the miRNA Extraction Kit (cat. no. CWY113S; CWBio) or the HiScript II Q RT SuperMix for qPCR (+gDNA wiper) (cat. no. R223-01; Vazyme Biotech Co., Ltd.), in

Table I. RP11-196G11.6-siRNA and hsa-miR-376a-3p mimic sequences.

Name	Sequence (5'-3')
RP11-196G11.6-siRNA	S: GUCACUAGACAUCCUGAAA
	AS: UUUCAGGAUGUCUAGUGAC
Negative control-siRNA	S: UUCUCCGAACGUGUCACGU
	AS: ACGUGACACGUUCGGAGAA
hsa-miR-376a-3p mimic	S: AUCAUAGAGGAAAAUCCACGU
	AS: ACGUGGAUUUUCCUCUAUGAU
Negative control mimic	S: UCACAACCUCCUAGAAAGAGUAGA
	AS: UCUACUCUUUCUAGGAGGUUGUGA

S, sense; AS, anti-sense; miR, microRNA; siRNA, small interfering RNA.

accordance with the manufacturers' protocols. Subsequently, fluorescence qPCR was performed using a fluorescence PCR instrument with SuperStar Universal SYBR Master Mix (cat. no. CW3360M; CWBio), as follows: Pre-denaturation at 95˚C for 10 min; followed by 40 cycles of denaturation at 95˚C for 10 sec, annealing at 58˚C for 30 sec and extension at 72˚C for 30 sec. β-actin and U6 were employed as endogenous controls for lncRNA/mRNA and miRNA normalization, respectively, and the relative expression levels of each gene were calculated with the $2^{-\Delta\Delta Cq}$ method (25). The specific primer sequences were as follows: Forward (F), 5'-TGGCACCCAGCACAATGAA-3' and reverse (R), 5'-CTAAGTCATAGTCCGCCTAGAAGCA-3' for β-actin NM_001101.5); F, 5'-CCAAGAAGGGCACAGGGAA-3' and R, 5'-GGAGTGAATGGGTGGGAGTTT-3' for RP11-196G11.6 (ENST00000622229.1); F, 5'-CACCTCCATTGTCTTCCC-3' and R, 5'-CCACTACTGCCCATTTCC-3' for U47924.29 (ENST00000606539.1); F, 5'-GACTTGTCTTTCGGGTTC-3' and R, 5'-CCTGGCAGCAATACTTTA-3' for AC000068.10 (ENST00000608816.1); F, 5'-GATCAGCAGTTCGAGACCAGC-3' and R, 5'-CACCTCACGTCACCTTCCATAA-3' for RP3-508I15.9 (ENST00000423346.1); F, 5'-GCGTACTGCAGACGTGGCA-3' and R, 5'-AGTGCAGGGTCCGAGGTATT-3' for hsa-miR-509-3-5p (MIMAT0004975); F, 5'-GCGCGATCATAGAGGAAAATC-3' and R, 5'-AGTGCAGGGTCCGAGGTATT-3' for hsa-miR-376b-3p (MIMAT0002172) F, 5'-CGCGCGATCATAGAGGAAAAT-3' and R, 5'-AGTGCAGGGTCCGAGGTATT-3' for hsa-miR-376a-3p (MIMAT0000729); F, 5'-CTCGCTTCGGCAGCACA-3' and R, 5'-AACGCTTCACGAATTTGCGT-3' for U6 (cat. no. NR_004394.1).

Cell Counting Kit-8 (CCK-8) assay. The transfected cells were plated uniformly in 96-well plates at a density of 3,000 cells/well and cultured overnight. At the specified time, the culture medium was discarded and the medium was replaced with serum-free medium containing CCK-8 reagent (cat. no. C0041; Beyotime Institute of Biotechnology). After incubation for 2 h at 37˚C, the absorbance values of each well were determined at a wavelength of 450 nm using a microplate reader (cat. no. WD-2012B; Beijing Liuyi Biotechnology, Co., Ltd.).

Apoptosis detected using flow cytometry. Apoptosis was measured by flow cytometry using the Annexin V-FITC/PI Apoptosis Kit [cat. no. AP101-100-kit; Multisciences (Lianke) Biotech Co., Ltd.]. After digestion of SH-SY5Y or IMR-32 cells from a 6-well plate, a single-cell suspension with a concentration of $1x10^6$/well was prepared. After centrifugation at 450 x g for 3 min at 37˚C, the samples were washed twice with PBS. The cells were then resuspended in 300 μl precooled 1XBinding Buffer, 5 μl Annexin V-FITC and 10 μl PI were added to each well and mixed gently, and the cells were incubated for 10 min at room temperature in the dark. The changes in apoptosis were observed using a flow cytometer (NovoCyte 2060R; ACEA Biosciences; Agilent Technologies, Inc.). Data analysis was performed using FlowJo (version v10.9.0; BD Biosciences). Apoptotic cells were defined as the cell population positive for Annexin V-FITC and negative for PI (early apoptosis), or positive for both Annexin V-FITC and PI (late apoptosis).

Cell scratch assay for cell migration. The cells ($3x10^5$/well) were cultured in 6-well plates until they reached 80-90% confluence with normal morphology and stable growth kinetics. Subsequently, the cells were inoculated into 24-well plates and cultured overnight to ensure cell attachment. Scratches were then made perpendicular to the bottom of the well using a 200-μl pipette tip. The cells were then cultured in serum-free medium for 24 h and images were captured under a light microscope (BX43; Olympus Corporation). The cell migration rate was calculated using the following formula: Cell migration rate (%)=$[(A_0-A_{24})/A_0]$ x100. (A_0 refers to the initial wound area at 0 h; A_{24} indicates the remaining wound area at the measured 24 h).

Transwell assay for cell invasion. The cells were cultured until they reached 80-90% confluence with normal morphology and stable growth kinetics. Subsequently, the cells were resuspended in serum-free medium. A 500-μl aliquot of cell-specific medium supplemented with 10% FBS was added to the lower chamber of a 24-well Transwell invasion chamber (BioCoat® Matrigel® Invasion Chamber; 8-μm pore size; cat. no. 354480; Corning, Inc.). The upper chamber was seeded with a 300-μl cell suspension containing $5x10^4$ cells/well. After incubation in a 37˚C CO_2 incubator for 24 h, the chambers were removed, the medium was discarded and the cells were stained with 0.1% crystal violet for 1 h at 37˚. The unmigrated cells in the

upper chambers were removed with a cotton swab and the cells that had invaded the lower chambers observed under a light microscope (BX43; Olympus Corporation). After images were captured, the staining solution was removed, the samples were treated with 33% acetic acid and the absorbance value of each well was measured at 562 nm with an enzyme labeling instrument (cat. no. WD-2012B; Beijing Liuyi Biotechnology, Co., Ltd.).

Western blotting (WB). The cells were harvested, the culture medium was discarded and total protein was extracted with RIPA lysis buffer (cat. no. C1053; Beijing Applygen Technologies, Inc.). After centrifugation at 14,490 x g for 10 min at 4˚C, the supernatant was collected and total protein was quantified using a BCA protein quantification kit (cat. no. E-BC-K318-M; Wuhan Elabscience Biotechnology Co., Ltd.). After denaturation of the protein samples, the loading volume was calculated based on a protein amount of 20 μg/lane. SDS gel (10% separating gel and 5% stacking gel) electrophoresis was performed for 1.5 h, followed by constant flow of the membrane at 300 mA for 1 h. The PVDF membrane (cat. no. IPVH00010; MilliporeSigma) was sealed with 3% non-fat dry milk for 1 h at room temperature and incubated with primary antibodies against RING1 and YY1-binding protein (RYBP; cat. no. 68130-1-Ig; Proteintech Group, Inc.; 1:2,000), EGFR (cat. no. GB11084-2; Wuhan Servicebio Technology Co., Ltd.; 1:1,000), phosphorylated (p)-EGFR (cat. no. YP0086; ImmunoWay Biotechnology Company; 1:1,000), vimentin (cat. no. GB11192; Wuhan Servicebio Technology Co., Ltd.; 1:1,000), GAPDH (cat. no. HC301; TransGen Biotech Co., Ltd.; 1:2,000) and E-cadherin [cat. no. GB12868; Wuhan Servicebio Technology Co., Ltd.; 1:1,000] overnight at 4˚C. The following day, the PVDF membrane was incubated with the HRP-conjugated goat anti-rabbit IgG (H+L) (cat. no. GB23303; Wuhan Servicebio Technology Co., Ltd.; 1:2,000) or HRP-conjugated Goat Anti-Mouse IgG (H+L) (cat. no. GB23301; Wuhan Servicebio Technology Co., Ltd.; 1:2,000) secondary antibody for 2 h at room temperature. The membrane was washed with 1X TBS-0.1% Tween buffer. Subsequently, the PVDF membrane was incubated with SuperSignal® West Pico Chemiluminescent Substrate (cat. no. RJ239676; Thermo Fisher Scientific, Inc.) and imaged using an ultra-high sensitivity chemiluminescence imaging system (Tanon-5200; Tanon Science and Technology Co., Ltd.). Semi-quantitative analysis was performed using Image Lab software (version 6.0; Bio-Rad Laboratories, Inc.).

Dual-luciferase reporter gene assay. In the dual-luciferase reporter gene assay, the wild-type (WT) and mutant (MUT) binding sequences of RP11-196G11.6 or RYBP 3'-UTR were cloned into the pmirGLO vector (Promega Corporation). The 239T cells were seeded in 24-well plates and were co-transfected with the following sequences using Lipofectamine 3000: i) To assess the RP11-196G11.6-miR-376a-3p interaction, cells were co-transfected with WT-RP11 vector + miR-376a-3p mimic, WT-RP11 vector + NC mimic, MUT-RP11 vector + miR-376a-3p mimic or MUT-RP11 vector + NC mimic; ii) to assess the miR-376a-3p-RYBP interaction, cells were co-transfected with WT-RYBP vector + miR-376a-3p mimic, WT-RYBP vector + NC mimic, MUT-RYBP vector + miR-376a-3p mimic or MUT-RYBP vector + NC mimic. WT-RP11-196G11.6-pmirGLO, MUT-RP11-196G11.6-pmirGLO, WT-RYBP-pmirGLO and MUT-RYBP-pmirGLO were obtained from ZHBY Biotechnology Co., Ltd. After transfection according to the experimental protocol of the dual-luciferase reporter gene assay kit (cat. no. RG027; Beyotime Institute of Biotechnology), the cells were cultured for 24 h. The medium was discarded and the remaining medium was washed with PBS. The supernatant was collected after the cells were lysed with passive lysis buffer (cat. no. RG027; Beyotime Institute of Biotechnology) Firefly and *Renilla* luciferase activities were measured sequentially using a chemiluminescence device (Glomax® 20/20 Luminometer; Promega Corporation) and the ratio of the two was calculated as relative luciferase activity.

Statistical analysis. Statistical analysis and the visualization of experimental data were performed using IBM SPSS software (version 22.0; IBM Corp.). Measurement data that follow a normal distribution are presented as the mean ± SD. For comparisons among multiple groups, one-way ANOVA followed by Tukey's post hoc test was used. For comparisons between two groups, unpaired Student's t-test was employed. Pearson's correlation coefficient was used when both variables followed a normal distribution. For variables that deviated from normality or were ordinal in nature, Spearman's rank correlation coefficient was applied. $P<0.05$ was considered to indicate a statistically significant difference. All experiments were performed with a minimum of three independent replicates. A graphical abstract for the present study is available in Fig. S1.

Results

Analysis of DElncRNAs in tumor tissues and DTC samples. First, an NB transcriptome sequencing dataset was downloaded from the GEO (accession no. GSE94035). Different NB samples (tumor samples and DTC samples with and without MYCN amplification) were analyzed at the molecular level. Using PCA, a clear distinction between tumor and DTC samples, and between $MYCN^+$ and $MYCN^-$ tumor samples was identified, but PCA was unable to distinguish between $MYCN^+$ and $MYCN^-$ DTC samples (Fig. 1B). The PCA results suggested that MYCN may serve a key role in tumor growth. Therefore, the DEGs between $MYCN^+$ and $MYCN^-$ samples were analyzed, and a total of 4,551 DEGs were detected in tumors (2,230 upregulated and 2,321 downregulated), whereas 2,714 DEGs were detected in DTCs (917 upregulated and 1,797 downregulated) (Fig. 1C). As shown in the Venn diagram, a total of 808 DEGs were detected, of which 339 were upregulated and 469 were downregulated (Fig. 1D). GO enrichment analysis revealed the GO terms that were most enriched in DEGs. As shown in Fig. 1E, specific upregulated DEGs regulated by MYCN in DTCs were enriched in 'extracellular matrix disassembly', 'collagen catabolic process', 'cellular response to cAMP', 'positive regulation of vasodilation' and 'axon guidance'. Downregulated DEGs in DTCs were enriched in 'cytokine-mediated signaling pathway', 'type I interferon-mediated signaling pathway', 'immune response' and 'inflammatory response'. These biological processes were associated with NB metastasis and invasion.

Next, the lncRNAs among the DEGs were analyzed. Using PCA, a clear distinction was identified between tumor samples and DTC samples, and between $MYCN^+$ and $MYCN^-$ tumor samples, whereas $MYCN^+$ and $MYCN^-$ DTC samples could not be distinguished (Fig. 1F). In addition, 1,110 DElncRNAs were identified in tumors (758 upregulated and 352 downregulated), whereas 793 DElncRNAs were identified in DTCs (231 upregulated and 562 downregulated) (Fig. 1G). Venn diagrams of the upregulated and downregulated lncRNAs in $MYCN^+$ tumor and DTC samples revealed that 73 DElncRNAs were co-upregulated and that 88 DElncRNAs were co-downregulated (Fig. 1H). WGCNA and co-expression analysis were analyzed between DElncRNAs and DEmRNAs in tumor and DTC samples (Fig. 1I). The results demonstrated that MYCNOS, XLOC-1045657, SNHG19, AC012123.1 and SNHG8 were the primary DElncRNAs in DTCs, whereas MYCNOS, EPB41L4A-AS1, RP11-92J19.3 and ZFAS1 were the primary DElncRNAs in tumors. The top 10 most enriched GO terms by DEmRNAs co-expressed with DElncRNAs are shown in Fig. 1J, which include a large number of signaling pathways associated with inflammation/immunity. These findings indicated that DElncRNA may serve a role in the progression of NB via immune-related pathways.

Analysis of DElncRNAs associated with Tregs and Tfhs. CIBERSORT was used to analyze the proportion of each immune cell type in $MYCN^+$ and $MYCN^-$ tumor and DTC samples (Fig. 2A). Based on the magnitude of intergroup differences between $MYCN^+$ and $MYCN^-$ samples in both tumor and DTC samples. Tregs demonstrated the highest proportion in the tumor-nonamplified group, whereas Tfhs were most abundant in the tumor-amplified group. By contrast, other cell types such as monocytes/macrophages showed minimal differences between groups. PCA revealed that the different types of cells clearly differentiated between the DTC and tumor samples, but the $MYCN^+$ samples and $MYCN^-$ samples were indistinguishable (Fig. 2B). Fig. 2C and D display the specific proportions of Tregs and Tfhs in the four types of samples. In DTC samples, there was no significant difference in the proportions of Tregs or Tfhs between $MYCN^+$ and $MYCN^-$ samples. However, in tumor samples, the proportion of Tregs in $MYCN^+$ samples were markedly lower compared with that in $MYCN^-$ samples, whereas the proportion of Tfhs in $MYCN^+$ samples was markedly higher compared with that in $MYCN^-$ samples.

Spearman's rank correlation coefficient was further calculated on the basis of the expression level of DElncRNAs and the ratio of Tregs to Tfhs, and 15 lncRNAs were shown to be associated with Tfhs, while two lncRNAs were associated with Tregs. The lncRNA-immune cell infiltration networks were constructed with Cytoscape (Fig. 2E), which revealed the lncRNAs associated with Tregs and Tfhs. Fig. 2F displays the expression levels of the top four DElncRNAs (U47924.29, AC000068.10, RP3-508I15.9 and RP11-196G11.6) associated with Tfh infiltration as determined by Spearman's rank correlation analysis. In DTC samples, there was no notable change in the expression levels of these four lncRNAs between the $MYCN^+$ and $MYCN^-$ samples. However, in tumor samples, the expression levels of these lncRNAs were markedly higher in $MYCN^+$ samples compared with those in $MYCN^-$ samples. The present study findings suggested that these four lncRNAs may be associated with NB tumor growth as well as immune infiltration. Next, the expression levels of these four lncRNAs were verified in $MYCN^+$ and $MYCN^-$ cells using RT-qPCR. It was identified that only RP11-196G11.6 exhibited successful amplification and showed high expression in $MYCN^+$ cells, while the other three lncRNAs failed to amplify, exhibiting delayed amplification profiles and aberrant dissociation curves, likely attributable to their inherently low expression levels in NB cells, which precluded further validation (Fig. S2). Thus, RP11-196G11.6 was selected for subsequent experimentation.

RP11-196G11.6 is highly expressed in $MYCN^+$ NB tumor tissues and $MYCN^+$ cells. First, the expression of RP11-196G11.6 was examined in $MYCN^+$ and $MYCN^-$ NB tumor tissues using FISH. According to the present study findings (Fig. 3A), RP11-196G11.6 was highly expressed in $MYCN^+$ NB tumor tissues. Next, the expression levels of RP11-196G11.6 were examined in $MYCN^-$ (SH-SY5Y) and the $MYCN^+$ (IMR-32) NB cell lines by RT-qPCR. The results revealed that the expression levels of RP11-196G11.6 were significantly higher in IMR-32 cells compared with those in SH-SY5Y cells (Fig. 3B). These results indicated that RP11-196G11.6 may be highly expressed in $MYCN^+$ NB tumor tissues and cells.

RP11-196G11.6 inhibits the viability, migration and invasion of NB cells. si-RP11 was transfected into IMR-32 cells and oe-RP11 was transfected into SH-SY5Y cells; subsequently, RT-qPCR confirmed that siRNA transfection significantly downregulated RP11-196G11.6 expression in IMR-32 cells, whereas transfection with oe-RP11 resulted in substantial upregulation of RP11-196G11.6 in SH-SY5Y cells, thereby validating the successful knockdown and overexpression of this lncRNA (Fig. 3C). The results of the CCK-8 assay (Fig. 3D) revealed that RP11-196G11.6 knockdown increased IMR-32 cell viability, whereas RP11-196G11.6 overexpression decreased the viability of SH-SY5Y cells. Flow cytometry (Fig. 3E and F) revealed that RP11-196G11.6 downregulation significantly inhibited IMR-32 apoptosis, whereas RP11-196G11.6 upregulation significantly increased SH-SY5Y apoptosis. The results of the cell scratch assay (Fig. 4A and B) revealed that RP11-196G11.6 downregulation promoted IMR-32 cell migration, whereas RP11-196G11.6 upregulation inhibited SH-SY5Y cell migration. Furthermore, the results of the Transwell assay (Fig. 4C and D) revealed that RP11-196G11.6 downregulation promoted IMR-32 cell invasion, whereas RP11-196G11.6 upregulation inhibited SH-SY5Y cell invasion. These results indicated that RP11-196G11.6 knockdown could promote NB cell viability, migration and invasion, whereas RP11-196G11.6 upregulation may inhibit these processes.

Next, the expression levels of the epithelial-mesenchymal transition (EMT)-related proteins, vimentin, E-cadherin, EGFR and p-EGFR, were detected in NB cells by WB. The results in IMR-32 cells (Fig. 4E and F) revealed that the downregulation of RP11-196G11.6 significantly decreased the protein expression levels of E-cadherin, and significantly increased the protein expression levels of vimentin and p-EGFR/EGFR. By contrast, the results in SH-SY5Y cells (Fig. 4G and H) revealed that the upregulation of

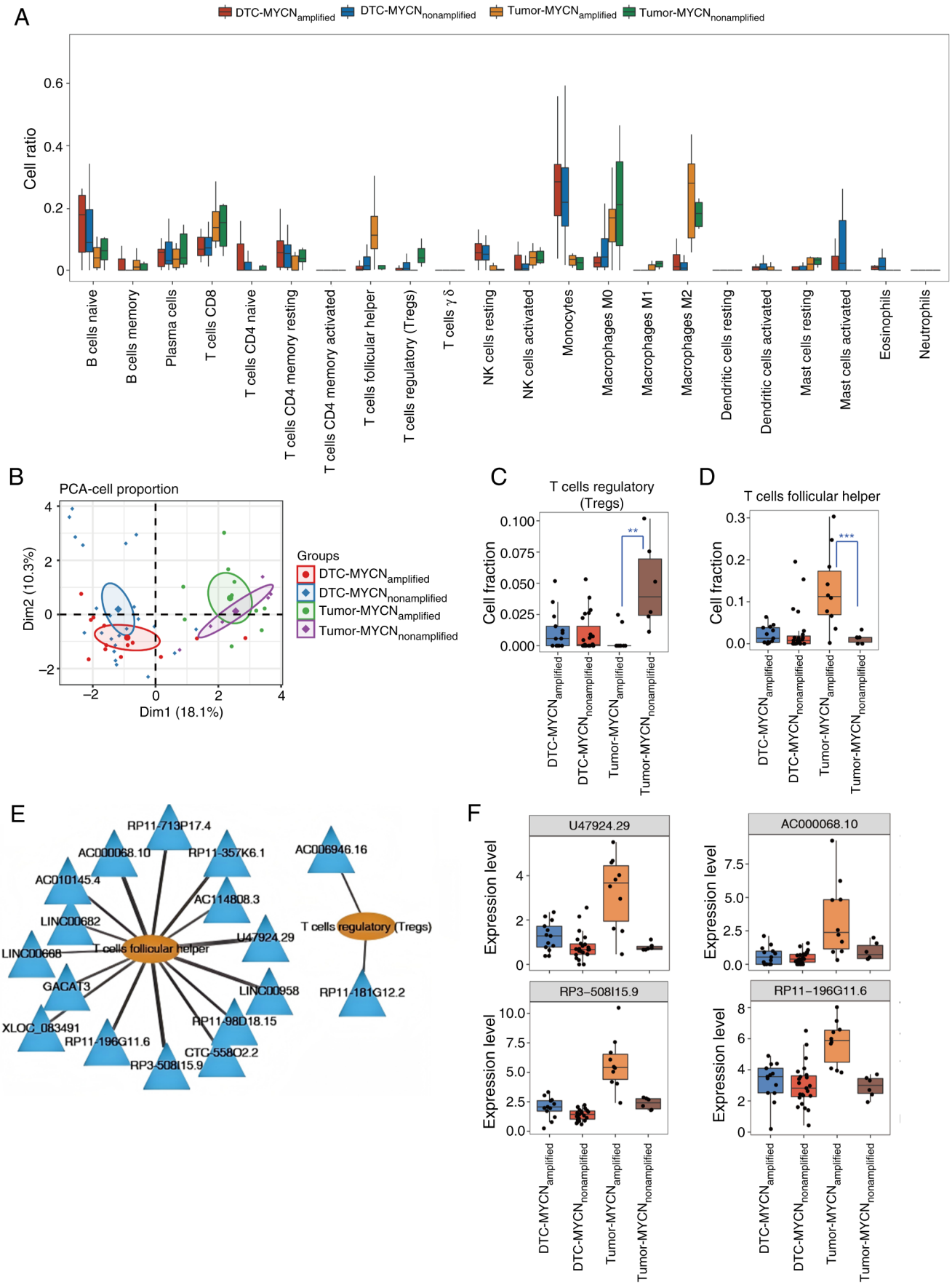

Figure 2. Analysis of DElncRNAs associated with Tregs and Tfhs. (A) CIBERSORT analysis of the proportion of each immune cell type in MYCN^{+} and MYCN^{-} samples from tumors and DTCs. (B) PCA of the different types of cells. (C) Specific proportions of Tregs in the four types of samples. **P<0.01 vs. Tumor-MYCN$_{nonamplified}$. (D) Specific proportions of Tfhs in the four types of samples. ***P<0.001 vs. Tumor-MYCN$_{nonamplified}$. (E) lncRNA-immune cell infiltration networks. (F) Expression levels of four DElncRNAs associated with Tfh infiltration. lncRNA, long non-coding RNA; DElncRNA, differentially expressed lncRNA; DTC, disseminated tumor cell; Treg, regulatory T cell; Tfh, T follicular helper cell; PCA, principal component analysis.

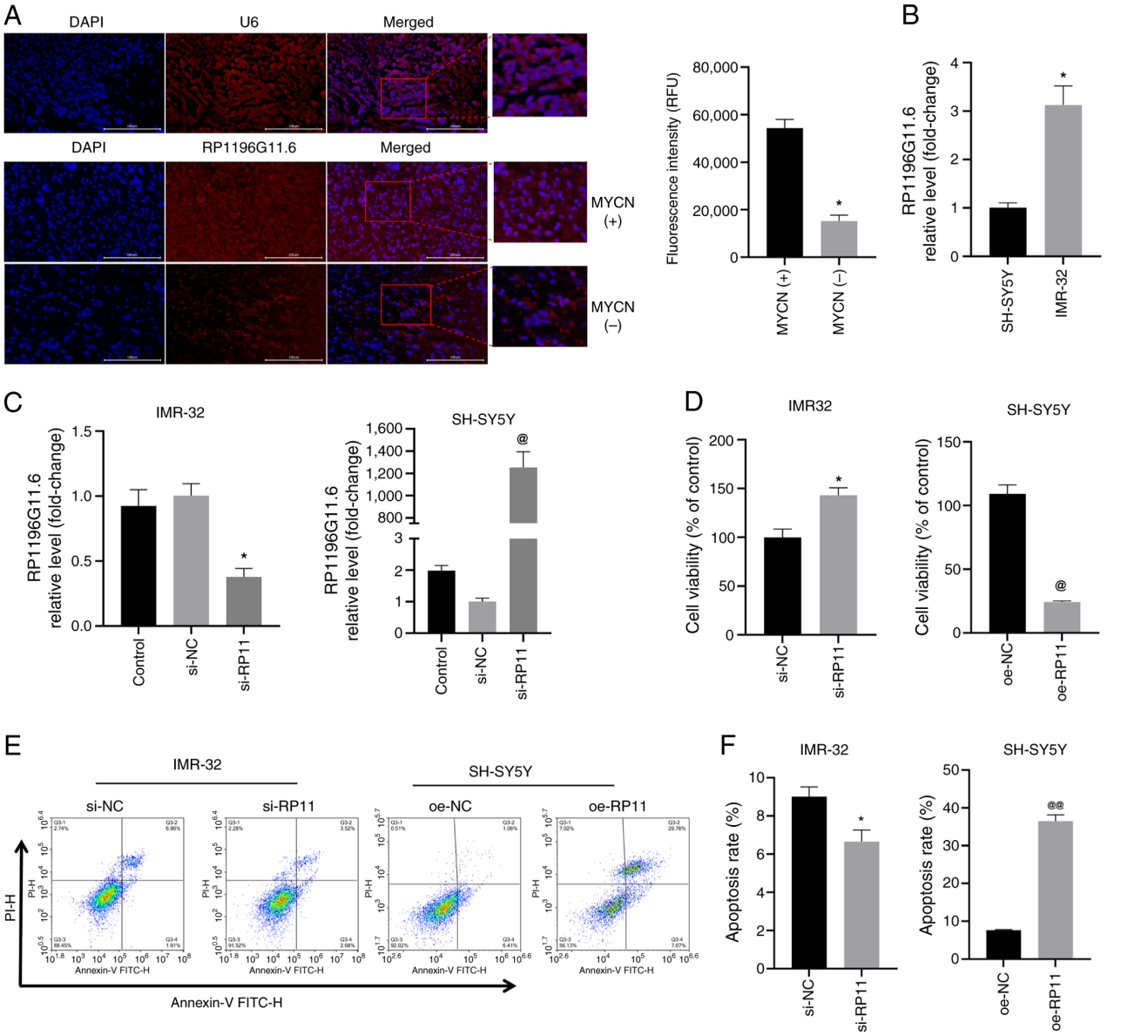

Figure 3. RP11is highly expressed in MYCN$^+$ NB tumor tissues and MYCN$^+$ NB cells, and RP11 upregulation inhibits NB cell viability. (A) FISH analysis revealed the expression level of RP11 in MYCN$^+$ and MYCN$^-$ NB tumor tissue specimens (scale bar, 100 μm; U6, control probe). *P<0.05 vs. MYCN$^+$ group. (B) Quantification of RP11 levels in SH-SY5Y and IMR-32 cells by reverse transcription-quantitative PCR. *P<0.05 vs. SH-SY5Y. (C) Quantification of RP11 levels in IMR-32 cells following transfection with si-RP11 and RP11 levels in SH-SY5Y cells following transfection with oe-RP11. *P<0.05 vs. si-NC, $^@$P<0.05 vs. oe-NC. (D) Viability of IMR-32 and SH-SY5Y cells was assessed using a Cell Counting Kit-8 assay. *P<0.05 vs. si-NC, $^@$P<0.05 vs. oe-NC. (E) Levels of apoptosis were assessed using flow cytometry in IMR-32 and SH-SY5Y cells. (F) Apoptosis rate of IMR-32 and SH-SHY5Y cells *P<0.05 vs. si-NC or $^{@@}$P<0.01 vs. oe-NC. RP11, RP11-196G11.6; si, small interfering; oe, overexpression; NB, neuroblastoma; FISH, fluorescence *in situ* hybridization; NC, negative control.

RP11-196G11.6 significantly increased the protein expression levels of E-cadherin, but significantly decreased the protein expression levels of vimentin and p-EGFR/EGFR. These results indicated that the upregulation of RP11-196G11.6 may inhibit the viability, migration and invasion of NB cells, and promote their apoptosis.

RP11-196G11.6 targets and inhibits the expression of miR-376a-3p in NB cells. miRanda predicted that the following three miRNAs could potentially bind to RP11-196G11.6: i) miR-376b-3p ii) miR-509-3-5p and iii) miR-376a-3p. These predictions were confirmed by RT-qPCR, which revealed that miR-376b-3p and miR-509-3-5p failed to amplify, exhibiting delayed amplification profiles and aberrant dissociation curves, likely attributable to their inherently low expression levels in NB cells, which could not be further validation (Fig. S3). However, it was revealed that the downregulation of RP11-196G11.6 significantly increased the expression levels of miR-376a-3p in IMR-32 cells whereas the upregulation of RP11-196G11.6 significantly decreased the expression levels of miR-376a-3p in SH-SY5Y cells (Fig. 5A). In addition, a dual-luciferase reporter gene assay (Fig. 5B) revealed that luciferase activity was significantly lower in the WT-RP11 + miR-376a-3p mimic group compared with that in the WT-RP11 + NC mimic group; however, the luciferase activity was not evidently different between the MUT-RP11 +

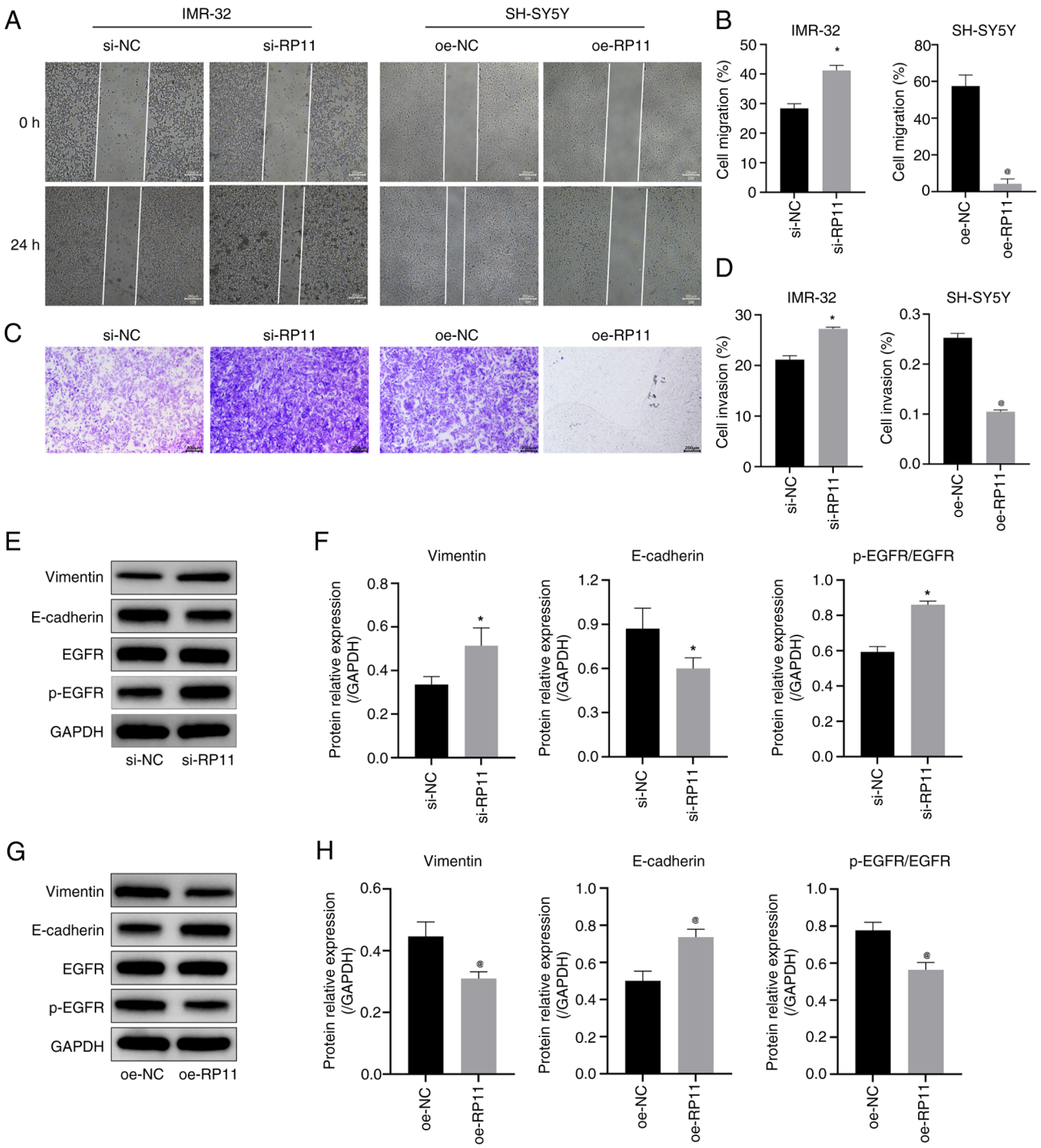

Figure 4. RP11 upregulation inhibits neuroblastoma cell migration and invasion. (A) Cell scratch assay results indicated that knockdown of RP11 expression promoted migration in IMR-32 cells and oe-RP11 suppressed migration in SH-SY5Y cells (scale bar, 200 μm). (B) Comparison of cell migration rates in IMR-32 and SH-SY5Y cells in the cell scratch assay. *P<0.05 vs. si-NC, @P<0.05 vs. oe-NC. (C) Transwell assay results indicated that knockdown of RP11 expression promoted invasion in IMR-32 cells and oe-RP11-196G11.6 suppressed invasion in SH-SY5Y cells (scale bar, 200 μm). (D) Quantitative analysis of cell invasion rate in the Transwell assay. *P<0.05 vs. si-NC, @P<0.05 vs. oe-NC. (E) Representative WB images in IMR-32 cells. (F) Expression levels of vimentin, E-cadherin and p-EGFR/EGFR in IMR-32 cells *P<0.05 vs. si-NC. (G) Representative WB images in SH-SY5Y cells. (H) Expression levels of vimentin, E-cadherin and p-EGFR/EGFR protein in SH-SY5Y cells. @P<0.05 vs. oe-NC. RP11, RP11-196G11.6; si, small interfering; oe, overexpression; WB, western blotting; p-, phosphorylated; NC, negative control.

NC group and the MUT-RP11 + mimic group. These results indicated that RP11-196G11.6 could target and inhibit the expression of miR-376a-3p. Using miRDB prediction, RYBP was identified as a downstream target gene of miR-376a-3p and RYBP has been confirmed to be associated with tumor suppression (26-28), including in hepatocellular carcinoma, colorectal cancer and lung cancer. Therefore, the protein expression levels of RYBP in cells was assessed by WB. The results revealed that the downregulation of RP11-196G11.6 significantly decreased the protein levels of RYBP in IMR-32 cells whereas the upregulation of RP11-196G11.6 significantly increased the protein levels of RYBP in SH-SY5Y cells

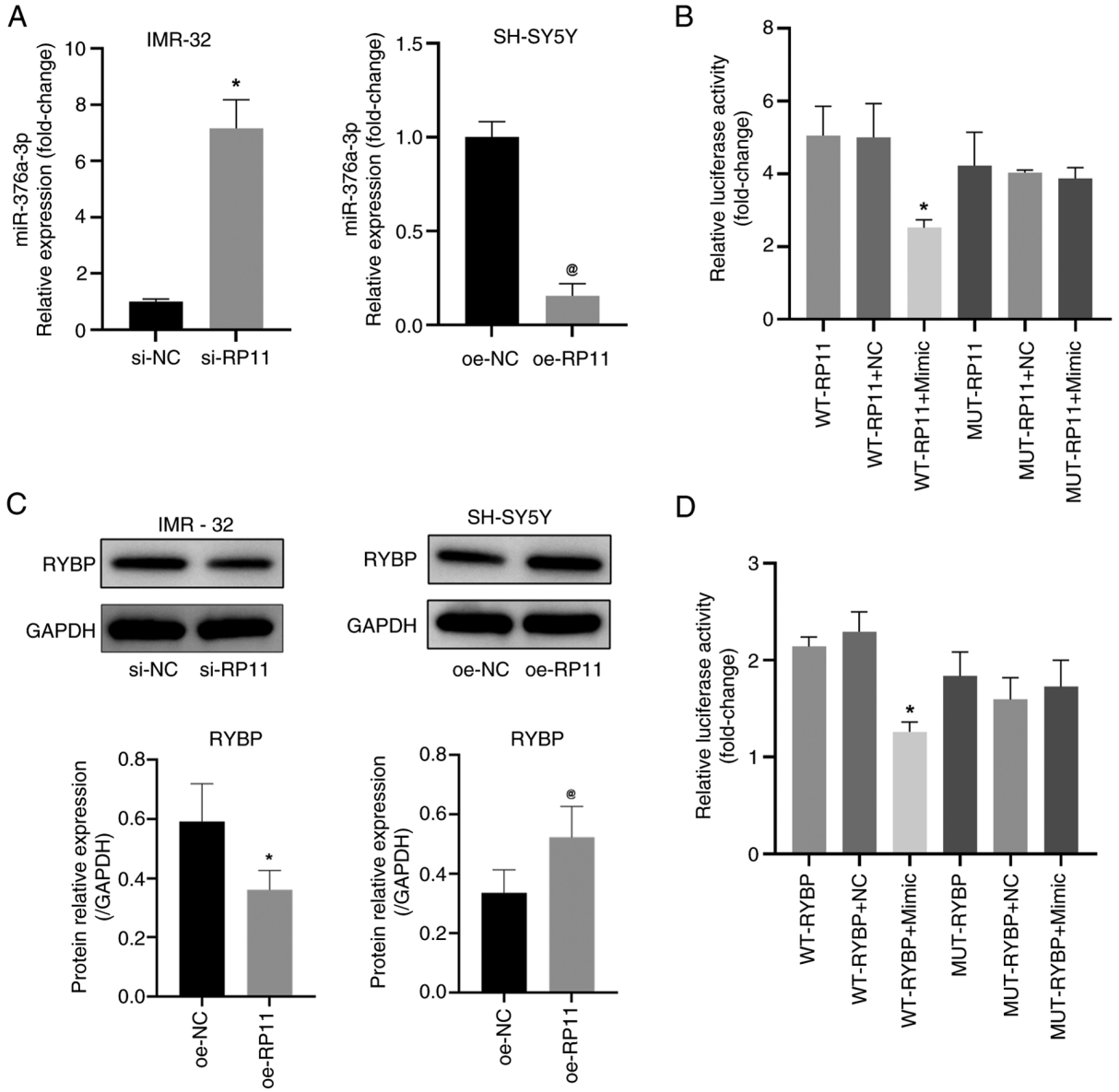

Figure 5. RP11 inhibits miR-376a-3p expression in neuroblastoma cells. (A) Quantification of miR-376a-3p levels in IMR-32 cells following transfection with si-RP11 and in SH-SY5Y cells following transfection with oe-RP11. *P<0.05 vs. si-NC, @P<0.05 vs. oe-NC. (B) Luciferase reporter assay was performed to measure the activity of the WT or MUT RP11 3'UTR vector in 293T cells that were co-transfected with either miR-376a-3p or NC mimics. *P<0.05 vs. WT-RP11 + NC. (C) RYBP protein levels detected by WB in IMR-32 and SH-SY5Y cells. *P<0.05 vs. si-NC, @P<0.05 vs. oe-NC. (D) Luciferase reporter assay was performed to measure the activity of the WT or MUT RYBP 3'UTR vector in 293T cells that were co-transfected with either miR-376a-3p or NC mimics. *P<0.05 vs. WT-RYBP + NC. RP11, RP11-196G11.6; si, small interfering; oe, overexpression; NC, negative control; WB, western blotting; WT, wild-type; RYBP, RING1 and YY1-binding protein; MUT, mutant; miR-376a-3p, microRNA-376a-3p.

(Fig. 5C). The targeting relationship between miR-376a-3p and RYBP was further verified using the dual-luciferase reporter gene assay. Compared with that in the WT-RYBP + NC mimic group, luciferase activity was significantly lower in the WT-RYBP + miR-376a-3p mimic group; however, the luciferase activity was not evidently different between the MUT-RYBP + NC group and the MUT-RYBP + mimic group (Fig. 5D). These results suggested that miR-376a-3p can bind to RYBP.

RP11-196G11.6 inhibits NB cell viability, migration and invasion by downregulating miR-376a-3p expression. To verify whether RP11-196G11.6 inhibits NB cell viability, migration and invasion via downregulation of miR-376a-3p, the effects of miR-376a-3p overexpression (Fig. S4) on the viability, migration and invasion of SH-SY5Y cells overexpressing RP11-196G11.6 was examined. The findings indicated that overexpression of miR-376a-3p reduced apoptosis and increased cell viability; the inhibitory effects of RP11-196G11.6 overexpression on cell viability (Fig. 6A) and the promotion of apoptosis (Fig. 6B) were partially reversed by miR-376a-3p overexpression. These results indicated that RP11-196G11.6 may inhibit NB cell viability and induce apoptosis by downregulating miR-376a-3p. In addition, miR-376a-3p overexpression promoted cell migration and invasion; it partially reversed the inhibitory effects of RP11-196G11.6 overexpression on cell migration and invasion (Fig. 6C-F). These findings suggested that RP11-196G11.6 could inhibit NB cell migration and invasion by downregulating miR-376a-3p.

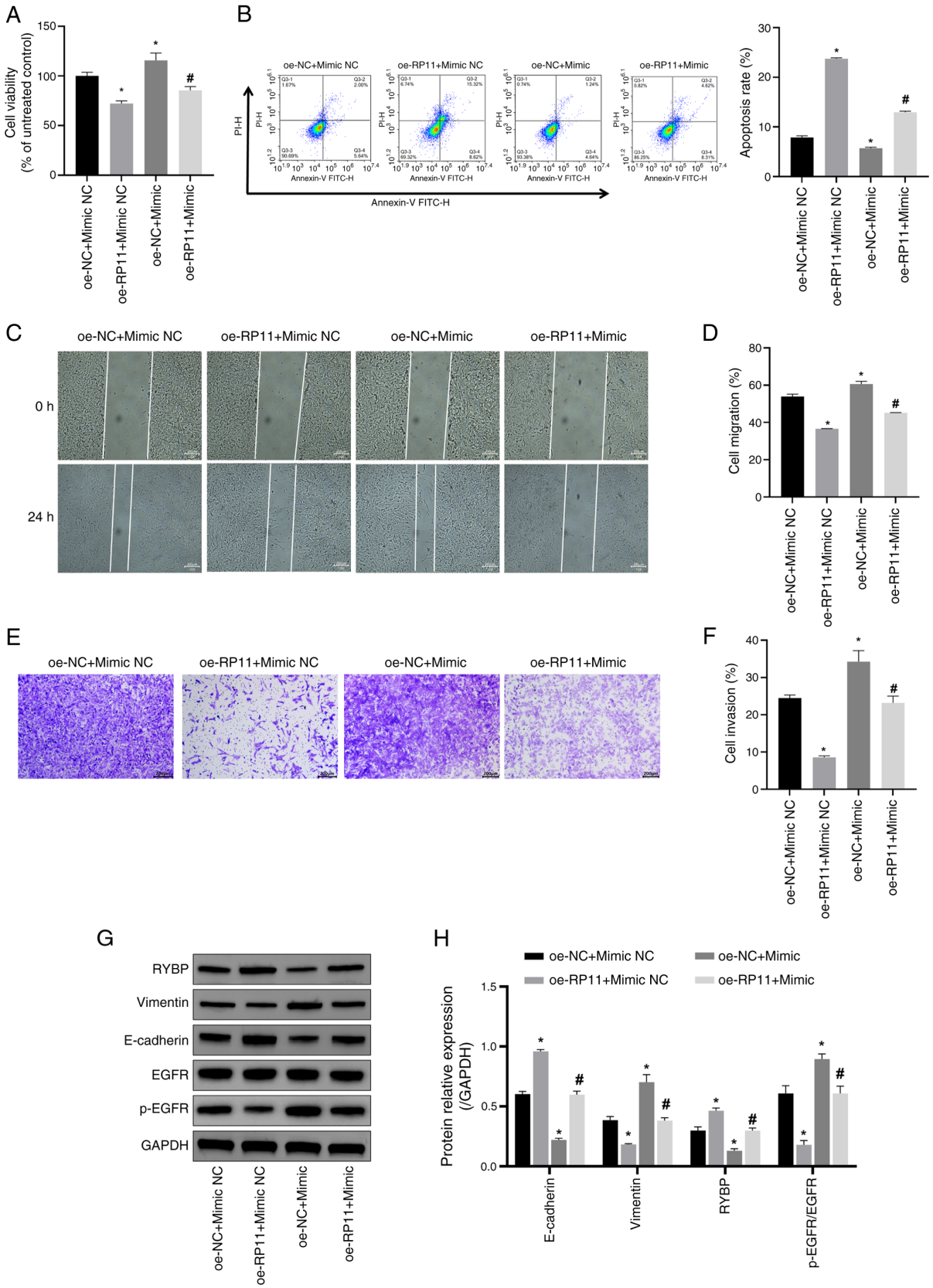

Figure 6. RP11 inhibits SH-SY5Y cell viability, migration and invasion by downregulating miR-376a-3p expression. (A) SH-SY5Y cell viability was assessed using a Cell Counting Kit-8 assay. *P<0.05 vs. oe-NC + mimic NC; #P<0.05 vs. oe-RP11 + mimic NC. (B) SH-SY5Y apoptosis was assessed using flow cytometry to assess the levels of SH-SY5Y apoptosis. *P<0.05 vs. oe-NC + mimic NC; #P<0.05 vs. oe-RP11 + mimic NC. (C) SH-SY5Y cell migration ability was detected using a cell scratch assay (scale bar, 200 μm). (D) Comparison of cell migration rates between the four groups in the cell scratch assay. *P<0.05 vs. oe-NC + mimic NC; #P<0.05 vs. oe-RP11 + mimic NC. (E) SH-SY5Y cell invasive ability was detected using a Transwell assay (scale bar, 200 μm). (F) Quantitative analysis of cell invasion rate in the four groups. *P<0.05 vs. oe-NC + mimic NC; #P<0.05 vs. oe-RP11 + mimic NC. (G) Representative western blotting image. (H) Semi-quantification of RYBP, vimentin, E-cadherin and p-EGFR/EGFR protein expression levels. *P<0.05 vs. oe-NC + mimic NC; #P<0.05 vs. oe-RP11 + mimic NC. oe, overexpression; NC, negative control; RP11, RP11-196G11.6; RYBP, RING1 and YY1-binding protein; miR-376a-3p, microRNA-376a-3p; p-, phosphorylated.

Next, the expression levels of the EMT-related proteins (vimentin, E-cadherin, EGFR, and p-EGFR) and RYBP in SH-SY5Y cells were detected by WB. The results revealed that, compared with in the oe-RP11 + Mimic NC group, miR-376a-3p overexpression in the oe-RP11 + Mimic downregulated the protein expression levels of RYBP and E-cadherin, but increased the protein expression levels of vimentin and p-EGFR/EGFR (Fig. 6G and H). Notably, miR-376a-3p overexpression partially reversed the effects of RP11-196G11.6 overexpression on the expression levels of RYBP, vimentin, E-cadherin and p-EGFR/EGFR.

Discussion

NB is one of the most common extracranial solid tumors in children, with notable heterogeneity and prognostic variability (29,30). MYCN amplification is a key molecular hallmark of NB, and is closely associated with tumor progression and poor prognosis (31). As lncRNAs serve a key role in NB (32), the molecular mechanism of action of lncRNAs remains to be further explored. In the present study, different NB samples were explored via bioinformatics analysis to identify MYCN-related DElncRNAs and analyze their potential roles in NB development. The results revealed high expression of RP11-196G11.6 in MYCN-amplified NB cells and further confirmed the effects of RP11-196G11.6-mediated miR-376a-3p and its downstream target gene RYBP on NB cell viability, migration and invasion.

First, MYCN-regulated Tregs and Tfhs were identified via CIBERSORT analysis. Subsequently, using Spearman's rank correlation analysis of the expression levels of DElncRNAs and the ratios of Tregs and Tfhs, DElncRNAs that were closely associated with Tregs and Tfhs were identified, and RP11-196G11.6 was selected as the focus of the present study. lncRNAs may influence the immune response by the following two mechanisms: i) lncRNAs regulate the innate immune response; and ii) lncRNAs regulate T-cell activation, development and differentiation (33).

Amplification of MYCN was among the earliest genetic hallmarks identified in NB and remains one of the most robust predictors of poor prognosis (34). Functionally, MYCN operates as both a transcription factor and a key oncogenic driver in this malignancy. As a member of the bHLH-LZ transcription factor family, MYCN binds canonical E-box motifs to activate proliferation-related targets, including ID2, ODC1 and MAD2, while concurrently suppressing neuronal differentiation pathways (35). MYCN exerts potent anti-apoptotic effects by upregulating the pro-survival proteins Bcl-2 and MCL-1, and by downregulating TP73, thereby attenuating the p53 pathway (36). Epigenetically, MYCN recruits the histone methyltransferase G9a and histone deacetylases 1 and 2, resulting in elevated histone H3 lysine 9 dimethylation and histone H3 lysine 27 trimethylation at both the ARID3B and MYCN promoters, and consequent transcriptional silencing of these loci (37). *In vivo* evidence was provided by the tyrosine hydroxylase-MYCN transgenic mouse model, in which restricted overexpression of MYCN within the sympathetic nervous system alone was sufficient to induce rapidly fatal NB, thereby establishing MYCN as a key oncogenic driver in this disease (38). In the present study, RP11-196G11.6 was highly expressed in MYCN-amplified cells, implying a functional association with MYCN. Previous data have indicated that MYCN can directly activate the transcription of multiple lncRNAs, such as CCAT1-L, H19 and HOTAIR (39); therefore, the elevated expression of RP11-196G11.6 may reflect direct transcriptional activation by MYCN. Nevertheless, it remains plausible that MYCN does not bind the RP11-196G11.6 locus directly but instead induces other transcription factors that indirectly de-repress or activate RP11-196G11.6 transcription.

Functional experiments in the present study confirmed that the downregulation of RP11-196G11.6 promoted the malignant phenotype of MYCN-amplified cells, whereas its overexpression suppressed the viability, migration and invasion of non-amplified cells. This result is consistent with previous studies, which demonstrated that MYCN can drive tumor progression by directly or indirectly regulating lncRNA expression. For example, the expression levels of LINC00839 in MYCN-amplified NB have been shown to be positively correlated with MYCN amplification, advanced INSS staging and worse prognosis. In *in vitro* experiments, silencing LINC00839 was demonstrated to inhibit cell proliferation, migration, invasion and EMT (40). The results of the present study suggested that RP11-196G11.6 serves a key regulatory role in the viability, migration and invasion of NB cells under different MYCN amplification states.

miR-376a-3p serves a key role in the malignant progression of several tumors. For example, in acute myeloid leukemia (AML), miR-376a-3p serves an inhibitory role in AML progression by targeting the metallothionein-1X gene, increasing apoptosis and inhibiting cell proliferation (41). In addition, miR-376a-3p serves a key role in colorectal cancer (CRC). Titin-antisense RNA1 (TTN-AS1), a lncRNA, sponges miR-376a-3p, which upregulates the expression of Krüppel-like factor 15 and promotes the progression of CRC. By inhibiting miR-376a-3p, TTN-AS1 can increase the proliferation and invasion of CRC cells (42). Similarly, in thyroid cancer, miR-376a-3p has been identified to be inhibitory. The lncRNA LINC00488 regulates the expression of paraoxonase 2, and promotes the proliferation and migration of thyroid cancer cells by binding to miR-376a-3p, whereas the overexpression of miR-376a-3p can inhibit these processes (43). However, in NB, to the best of our knowledge, there is no clear information regarding the role of miR-376a-3p. In the present study, it was identified that miR-376a-3p overexpression promoted SH-SY5Y cell viability, migration and invasion. Further molecular mechanism studies revealed that RP11-196G11.6 regulates the activity of its downstream target gene RYBP by targeting and inhibiting the expression of miR-376a-3p. The dual luciferase assay results confirmed the interaction between RP11-196G11.6 and miR-376a-3p, and revealed that miR-376a-3p was able to directly target the RYBP gene. Notably, the subsequent experiments revealed that the overexpression of miR-376a-3p partially reversed the inhibition of SH-SY5Y cell viability, migration and invasion induced by RP11-196G11.6 overexpression. These findings imply that RP11-196G11.6 may regulate the miR-376a-3p/RYBP pathway to inhibit NB progression.

Notably, CIBERSORT analysis revealed that RP11-196G11.6 expression was significantly correlated with the ratio of Tfhs in the tumor microenvironment. The enrichment of Tregs is often

associated with the immunosuppressive microenvironment and tumor immune escape (44,45), while Tfhs may influence the antitumor immune response by modulating B-cell function, which affects the antitumor immune response (46). Whether RP11-196G11.6 indirectly regulates immune cell infiltration through the miR-376a-3p/RYBP axis remains to be further explored. In addition, aberrant expression of RYBP may affect tumor cell-microenvironment interactions through epigenetic reprogramming, which provides a potential direction for future studies.

RYBP has been reported to inhibit cell proliferation, migration and invasion in a variety of tumors, in particular by regulating the EGFR signaling pathway (47,48). In lung cancer studies, RYBP suppresses tumor progression and metastasis by inhibiting EGFR signaling and EMT. As core EMT markers, vimentin and E-cadherin are key in tumor biology, where EMT enables cancer cells to acquire migratory, invasive and metastatic properties (49). E-cadherin, as a key epithelial cell adhesion molecule, is often markedly downregulated or absent during the EMT process, leading to the dissociation of intercellular junction structures, thus making tumor cells more likely to detach from the primary site and enter a migratory and invasive state (50). By contrast, vimentin, a mesenchymal cytoskeletal protein, is markedly upregulated during the EMT process. This change helps enhance the motility and morphological plasticity of cells, thereby promoting their invasive and metastatic potential (51). Particularly, overexpression of RYBP has been shown to reduce the phosphorylation level of EGFR and its downstream signaling molecules, thereby inhibiting cell proliferation and migration (52). In addition, RYBP expression has been identified to be negatively associated with tumor invasiveness, and to inhibit tumor cell proliferation and migration by suppressing the EGFR signaling pathway. These results implied that by controlling the EGFR signaling pathway, RYBP may have an inhibitory effect on a range of malignancies (53). The findings of the present study demonstrated that RP11-196G11.6 overexpression blocked the EGFR pathway and increased RYBP expression. Overexpression of RP11-196G11.6 suppressed vimentin protein expression and promoted E-cadherin protein expression. These findings suggest that by influencing the EGFR pathway and mediating EMT, the RP11-196G11.6/miR-376a-3p/RYBP axis may have an impact on the invasive metastasis of NB tumors.

Although the present study initially elucidated the function and mechanism of RP11-196G11.6, certain limitations still exist. The present study lacked the validation of clinical data and animal models, and was based on cell line models. Therefore, further external validation methods should be performed in the future. Second, it remains unclear as to whether RP11-196G11.6 is directly regulated by MYCN transcription and this requires further experimental verification. Lastly, whether RYBP inhibits the progression of NB by suppressing the EGFR signaling pathway still requires in-depth analysis. In addition, the role of RP11-196G11.6 in the prognosis of NB with MYCN amplification will be explored in future studies, with the aim of identifying additional potential markers for prognostic assessment.

In conclusion, to the best of our knowledge, the present study was the first to demonstrate the key function of RP11-196G11.6 in NB. Through the regulation of miR-376a-3p and its target gene RYBP, RP11-196G11.6 may promote apoptosis, and inhibit NB cell viability, migration and invasion. Therefore, RP11-196G11.6 could potentially be a novel target for therapeutic intervention in NB.

Acknowledgements

Not applicable.

Funding

The present study was supported in part by the Key Project of the National Key R&D Plan 'Research on Prevention and Control of Major Chronic Non-Communicable Diseases', the Ministry of Science and Technology of the People's Republic of China (grant nos. 2018YFC1313000 and 2018YFC1313004).

Availability of data and materials

The data generated in the present study may be requested from the corresponding author.

Authors' contributions

JZha was responsible for the overall conception and design of the present study and wrote the manuscript. KH and JZho performed most of the experiments and the data analysis. WL and FL collected the data. ZZ reviewed and revised the manuscript, and performed the bioinformatics analyses, including figure generation and statistical analysis. SW prepared research ideas, obtained funding and revised the manuscript, and was responsible for interpretation of the experimental findings and statistical analysis. JZHa and KH confirm the authenticity of all the raw data. All authors read and approved the final manuscript.

Ethics approval and consent to participate

The present study was approved by the Ethical Committee of Guizhou Provincial People's Hospital (approval no. 2025-104; Guizhou, China) and written informed consent was obtained from the parents of all participants before enrollment in the present study.

Patient consent for publication

Not applicable.

Competing interests

The authors declare that they have no competing interests.

References

1. Irwin MS and Park JR: Neuroblastoma: Paradigm for precision medicine. Pediatr Clin North Am 62: 225-256, 2015.
2. Suh E, Stratton KL, Leisenring WM, Nathan PC, Ford JS, Freyer DR, McNeer JL, Stock W, Stovall M, Krull KR, *et al*: Late mortality and chronic health conditions in long-term survivors of early-adolescent and young adult cancers: A retrospective cohort analysis from the childhood cancer survivor study. Lancet Oncol 21: 421-435, 2020.

3. Ponzoni M, Bachetti T, Corrias MV, Brignole C, Pastorino F, Calarco E, Bensa V, Giusto E, Ceccherini I and Perri P: Recent advances in the developmental origin of neuroblastoma: An overview. J Exp Clin Cancer Res 41: 92, 2022.
4. Körber V, Stainczyk SA, Kurilov R, Henrich KO, Hero B, Brors B, Westermann F and Höfer T: Neuroblastoma arises in early fetal development and its evolutionary duration predicts outcome. Nat Genet 55: 619-630, 2023.
5. Monclair T, Brodeur GM, Ambros PF, Brisse HJ, Cecchetto G, Holmes K, Kaneko M, London WB, Matthay KK, Nuchtern JG, *et al*: The international neuroblastoma risk group (INRG) staging system: An INRG task force report. J Clin Oncol 27: 298-303, 2009.
6. Castel V, García-Miguel P, Cañete A, Melero C, Navajas A, Ruíz-Jiménez JI, Navarro S and Badal MD: Prospective evaluation of the international neuroblastoma staging system (INSS) and the international neuroblastoma response criteria (INRC) in a multicentre setting. Eur J Cancer 35: 606-611, 1999.
7. Shimada H, Ambros IM, Dehner LP, Hata J, Joshi VV, Roald B, Stram DO, Gerbing RB, Lukens JN, Matthay KK and Castleberry RP: The international neuroblastoma pathology classification (the Shimada system). Cancer 86: 364-372, 1999.
8. Pinto NR, Applebaum MA, Volchenboum SL, Matthay KK, London WB, Ambros PF, Nakagawara A, Berthold F, Schleiermacher G, Park JR, *et al*: Advances in risk classification and treatment strategies for neuroblastoma. J Clin Oncol 33: 3008-3017, 2015.
9. Steliarova-Foucher E, Colombet M, Ries LAG, Moreno F, Dolya A, Bray F, Hesseling P, Shin HY and Stiller CA; IICC-3 contributors: International incidence of childhood cancer, 2001-10: A population-based registry study. Lancet Oncol 18: 719-731, 2017.
10. Diede SJ: Spontaneous regression of metastatic cancer: Learning from neuroblastoma. Nat Rev Cancer 14: 71-72, 2014.
11. Brodeur GM, Seeger RC, Schwab M, Varmus HE and Bishop JM: Amplification of N-myc in untreated human neuroblastomas correlates with advanced disease stage. Science 224: 1121-1124, 1984.
12. Ruiz-Pérez MV, Henley AB and Arsenian-Henriksson M: The MYCN protein in health and disease. Genes (Basel) 8: 113, 2017.
13. Huang M and Weiss WA: Neuroblastoma and MYCN. Cold Spring Harb Perspect Med 3: a014415, 2013.
14. Taniue K and Akimitsu N: The functions and unique features of LncRNAs in cancer development and tumorigenesis. Int J Mol Sci 22: 632, 2021.
15. Yang R, Liu N, Li T, Liu F, Zhang J, Zhao H, Zou L and He X: LncRNA AC142119.1 facilitates the progression of neuroblastoma by epigenetically initiating the transcription of MYCN. J Transl Med 21: 659, 2023.
16. Hsu CL, Yin CF, Chang YW, Fan YC, Lin SH, Wu YC, Huang HC and Juan HF: LncRNA SNHG1 regulates neuroblastoma cell fate via interactions with HDAC1/2. Cell Death Dis 13: 809, 2022.
17. Hu Z, Xu W, Wang H, Li M, Wang J, Sun C and Yang X: CARM1-induced lncRNA NEAT1 synchronously activates MYCN and GalNAcT-I to accelerate the progression of neuroblastoma. Gene 938: 149164, 2025.
18. Kim D, Pertea G, Trapnell C, Pimentel H, Kelley R and Salzberg SL: TopHat2: Accurate alignment of transcriptomes in the presence of insertions, deletions and gene fusions. Genome Biol 14: R36, 2013.
19. Robinson MD, McCarthy DJ and Smyth GK: edgeR: A bioconductor package for differential expression analysis of digital gene expression data. Bioinformatics 26: 139-140, 2010.
20. Liu S, Wang Z, Chen D, Zhang B, Tian RR, Wu J, Zhang Y, Xu K, Yang LM, Cheng C, *et al*: Annotation and cluster analysis of spatiotemporal- and sex-related lncRNA expression in rhesus macaque brain. Genome Res 27: 1608-1620, 2017.
21. Trapnell C, Roberts A, Goff L, Pertea G, Kim D, Kelley DR, Pimentel H, Salzberg SL, Rinn JL and Pachter L: Differential gene and transcript expression analysis of RNA-seq experiments with TopHat and Cufflinks. Nat Protoc 7: 562-578, 2012.
22. Sturm G, Finotello F and List M: Immunedeconv: An R package for unified access to computational methods for estimating immune cell fractions from bulk RNA-sequencing data. Methods Mol Biol 2120: 223-232, 2020.
23. Langfelder P and Horvath S: WGCNA: An R package for weighted correlation network analysis. BMC Bioinformatics 9: 559, 2008.
24. Xie C, Mao X, Huang J, Ding Y, Wu J, Dong S, Kong L, Gao G, Li CY and Wei L: KOBAS 2.0: A web server for annotation and identification of enriched pathways and diseases. Nucleic Acids Res 39 (Web Server Issue): W316-W322, 2011.
25. Livak KJ and Schmittgen TD: Analysis of relative gene expression data using real-time quantitative PCR and the 2(-Delta Delta C(T)) method. Methods 25: 402-408, 2001.
26. Tan K, Zhang X, Cong X, Huang B, Chen H and Chen D: Tumor suppressor RYBP harbors three nuclear localization signals and its cytoplasm-located mutant exerts more potent anti-cancer activities than corresponding wild type. Cell Signal 29: 127-137, 2017.
27. Zhu X, Yan M, Luo W, Liu W, Ren Y, Bei C, Tang G, Chen R and Tan S: Expression and clinical significance of PcG-associated protein RYBP in hepatocellular carcinoma. Oncol Lett 13: 141-150, 2017.
28. Morinaka T, Sakai N, Takayashiki T, Kuboki S, Takano S, Ohira G, Matsubara H and Ohtsuka M: RYBP contributes to improved prognosis in colorectal cancer via regulation of cell cycle, apoptosis and oxaliplatin sensitivity. Int J Oncol 63: 120, 2023.
29. Zafar A, Wang W, Liu G, Wang X, Xian W, McKeon F, Foster J, Zhou J and Zhang R: Molecular targeting therapies for neuroblastoma: Progress and challenges. Med Res Rev 41: 961-1021, 2021.
30. Qiu B and Matthay KK: Advancing therapy for neuroblastoma. Nat Rev Clin Oncol 19: 515-533, 2022.
31. Floros KV, Cai J, Jacob S, Kurupi R, Fairchild CK, Shende M, Coon CM, Powell KM, Belvin BR, Hu B, *et al*: MYCN-amplified neuroblastoma is addicted to iron and vulnerable to inhibition of the system Xc-/glutathione axis. Cancer Res 81: 1896-1908, 2021.
32. Vaid R, Thombare K, Mendez A, Burgos-Panadero R, Djos A, Jachimowicz D, Lundberg KI, Bartenhagen C, Kumar N, Tümmler C, *et al*: METTL3 drives telomere targeting of TERRA lncRNA through m6A-dependent R-loop formation: A therapeutic target for ALT-positive neuroblastoma. Nucleic Acids Res 52: 2648-2671, 2024.
33. Heward JA and Lindsay MA: Long non-coding RNAs in the regulation of the immune response. Trends Immunol 35: 408-419, 2014.
34. Otte J, Dyberg C, Pepich A and Johnsen JI: MYCN function in neuroblastoma development. Front Oncol 10: 624079, 2021.
35. Braoudaki M, Hatziagapiou K, Zaravinos A and Lambrou GI: MYCN in neuroblastoma: 'Old wine into new wineskins'. Diseases 78: 78, 2021.
36. Chen L and Tweddle DA: p53, SKP2, and DKK3 as MYCN target genes and their potential therapeutic significance. Front Oncol 28: 173, 2012.
37. Kobayashi K, Jakt LM and Nishikawa SI: Epigenetic regulation of the neuroblastoma genes, Arid3b and Mycn. Oncogene 32: 2640-2648, 2013.
38. Weiss WA, Aldape K, Mohapatra G, Feuerstein BG and Bishop JM: Targeted expression of MYCN causes neuroblastoma in transgenic mice. EMBO J 16: 2985-1995, 1997.
39. Winkle M, van den Berg A, Tayari M, Sietzema J, Terpstra M, Kortman G, de Jong D, Visser L, Diepstra A, Kok K and Kluiver J: Long noncoding RNAs as a novel component of the Myc transcriptional network. FASEB J 29: 2338-2346, 2015.
40. Zhang Q, Wei J, Li N and Liu B: LINC00839 promotes neuroblastoma progression by sponging miR-454-3p to Up-regulate NEUROD1. Neurochem Res 47: 2278-2293, 2022.
41. Xin X, Xu Z, Wei J and Zhang Y: MiR-376a-3p increases cell apoptosis in acute myeloid leukemia by targeting MT1X. Cancer Biol Ther 23: 234-242, 2022.
42. Wang Y, Jiang F, Xiong Y, Cheng X, Qiu Z and Song R: LncRNA TTN-AS1 sponges miR-376a-3p to promote colorectal cancer progression via upregulating KLF15. Life Sci 244: 116936, 2020.
43. Xie F, Li L, Luo Y, Chen R and Mei J: Long non-coding RNA LINC00488 facilitates thyroid cancer cell progression through miR-376a-3p/PON2. Biosci Rep 41: BSR20201603, 2021.
44. Shan F, Somasundaram A, Bruno TC, Workman CJ and Vignali DAA: Therapeutic targeting of regulatory T cells in cancer. Trends Cancer 8: 944-961, 2022.
45. Yan S, Zhang Y and Sun B: The function and potential drug targets of tumour-associated Tregs for cancer immunotherapy. Sci China Life Sci 62: 179: 186, 2019.
46. Overacre-Delgoffe AE, Bumgarner HJ, Cillo AR, Burr AHP, Tometich JT, Bhattacharjee A, Bruno TC, Vignali DAA and Hand TW: Microbiota-specific T follicular helper cells drive tertiary lymphoid structures and anti-tumor immunity against colorectal cancer. Immunity 54: 2812-2824.e4, 2021.
47. Zhou H, Li J, Zhang Z, Ye R, Shao N, Cheang T and Wang S: RING1 and YY1 binding protein suppresses breast cancer growth and metastasis. Int J Oncol 49: 2442-2452, 2016.

48. Xian Y, Wang L, Yao B, Yang W, Mo H, Zhang L and Tu K: MicroRNA-769-5p contributes to the proliferation, migration and invasion of hepatocellular carcinoma cells by attenuating RYBP. Biomed Pharmacother 118: 109343, 2019.
49. Ganesan K, Xu C, Wu S, Sui Y, Du B, Zhang J, Gao F, Chen J and Tang H: Ononin inhibits tumor bone metastasis and osteoclastogenesis by targeting mitogen-activated protein kinase pathway in breast cancer. Research (Wash D C) 7: 0553, 2024.
50. Zeng Y, Du W, Huang Z, Wu S, Ou X, Zhang J, Peng C, Sun X and Tang H: Hsa_circ_0060467 promotes breast cancer liver metastasis by complexing with eIF4A3 and sponging miR-1205. Cell Death Discov 9: 153, 2023.
51. Han M, Yang J, Chen P, Li S, Tang H, Fan H, Wang Y, Li X, Pan W, Koutouratsas V, *et al*: Isocucurbitacin B inhibits gliomas through the promotion of anoikis by targeting caveolin 1. Cancer Lett 629: 217873, 2025.
52. Dinglin X, Ding L, Li Q, Liu Y, Zhang J and Yao H: RYBP inhibits progression and metastasis of lung cancer by suppressing EGFR signaling and epithelial-mesenchymal transition. Transl Oncol 10: 280-287, 2017.
53. Tong AH, Tan J, Zhang JH, Xu FJ, Li FY and Cao CY: Overexpression of RYBP inhibits proliferation, invasion, and chemoresistance to cisplatin in anaplastic thyroid cancer cells via the EGFR pathway. J Biochem Mol Toxicol 33: e22241, 2019.